Journal of Cleaner Production 425 (2023) 138894

Contents lists available at ScienceDirect

Journal of Cleaner Production

journal homepage: www.elsevier.com/locate/jclepro

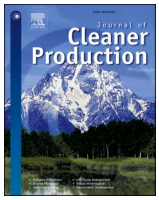

Properties of fly ash-based spray-applied fire resistive materials

Qingtao Huang [a], Zhong Tao [a,*], Zhu Pan [a], Laurel George [b], Richard Wuhrer [b], Maroun Rahme [c]

[a] Centre for Infrastructure Engineering, Western Sydney University, Penrith, NSW, 2751, Australia
[b] Advanced Materials Characterisation Facility, Western Sydney University, Parramatta, NSW, 2116, Australia
[c] Nu-Rock Technology Pty Ltd, Ryde, NSW, 2112, Australia

ARTICLE INFO

Handling Editor: Panos Seferlis

Keywords:
Fire insulation
Spray-applied fire resistive materials
Fly ash blended cement
Greenhouse gas emissions
Sustainability

ABSTRACT

Spray-applied fire-resistive materials (SFRMs) are one of the most commonly used passive fire protection materials due to their low thermal conductivity, lightweight, cost-effectiveness, and ease of application. Gypsum and Portland cement are commonly used in SFRMs to bind lightweight fillers and fibres. Due to the wide application of SFRMs, their production consumes large amounts of natural and non-renewable resources and contributes significantly to greenhouse gas emissions. This paper investigates the feasibility of using industrial by-products (e.g., fly ash) and waste materials (e.g., waste glass) to manufacture SFRMs with the aim of reducing the environmental impact. Accordingly, three SFRMs with different densities were developed utilising fly ash blended cement (FAC) and expanded glass. The use of FAC significantly reduced the use of Portland cement by 81% and achieved a 28-day compressive strength of 33.8–46.3 MPa for the binder. The developed SFRMs had average densities of 345 kg/m^3, 560 kg/m^3, and 698 kg/m^3 for low-, medium-, and high-density groups, respectively. The compressive strengths of the SFRMs ranged from 747 kPa to 888 kPa, 6188 kPa to 7314 kPa, and 2343 kPa to 3535 kPa for the corresponding three groups, respectively. Additionally, the bond strengths of the corresponding SFRMs are 14.4 kPa–19.3 kPa (low-density), 34 kPa–40.9 kPa (medium-density), and 51.5 kPa–85.1 kPa (high-density), respectively. All the tested SFRMs met the requirements for density, compressive strength, bond strength, and non-combustibility. The thermal properties of the developed SFRMs were comparable to those of commercially available cementitious-based SFRMs in the same density group. In addition, using FAC instead of Portland cement could reduce carbon emissions by 68.4% and save costs by 38.4% in the Australian context.

1. Introduction

Fire safety is a very important component of building design to avoid/reduce potential economic losses and ensure the life safety of occupants and firefighters. To achieve these purposes, active and passive fire protection systems are commonly used in designing buildings and other structures. Active fire protection systems, such as sprinklers and smoke alarms, have played an important role in detecting and suppressing fire and achieving the goals of fire safety. However, it is very costly to install and maintain active fire protection systems (Kodur et al., 2019). Meanwhile, the reliability of an active system could be compromised by a system failure or extreme events, such as earthquakes, explosions and impacts (Kodur and Arablouei, 2015). In contrast, passive fire protection systems (such as insulation boards, intumescent paints, and spray-applied fire-resistive materials) are very effective in reducing the structural temperature rise caused by fire (Braxtan and Pessiki, 2011). Among different passive fire protection systems, spray-applied fire-resistive materials (SFRMs) are commonly used to protect structural steel due to their low thermal conductivity, lightweight, cost-effectiveness, and ease of application (Islam and Rubieyat, 2018). It is well-known that structural steel is vulnerable to fire, as it starts to lose its yield stress at around 400 °C and retains approximately 50% of its strength at 600 °C (Jowsey and Scott, 2014). The application of SFRMs for protecting structural steel initiated in 1940s, aiming to significantly slow down the temperature rise of structural steel during a fire (Bentz, 2010).

Over many decades, numerous SFRM products have been developed worldwide, and the properties of some commercially available SFRMs are presented in Table 1. In general, SFRMs can be divided into three density groups: low density (240−352 kg/m^3), medium density (353−640 kg/m^3), and high density (641−750 kg/m^3) (ISOLATEK International, 2019; MasterFormat, 2011). Low-density SFRMs are

* Corresponding author.
E-mail address: z.tao@westernsydney.edu.au (Z. Tao).

https://doi.org/10.1016/j.jclepro.2023.138894
Received 18 June 2023; Received in revised form 12 August 2023; Accepted 3 September 2023
Available online 22 September 2023

typically used for concealed structural components (above ceilings or in walls) and are not suitable for outdoor weather conditions. Medium-density SFRMs are typically used for exposed structural components to achieve excellent fire resistance and serviceability, whereas high-density SFRMs are typically used in mechanical rooms and storage areas (Gewain et al., 2006).

Currently, gypsum and Portland cement are the primary binders used in SFRMs, accounting for approximately 50–75% of the total weight of the materials used for SFRM production. White et al. (2016) investigated the behaviour of gypsum-based medium-density SFRM at elevated temperatures. They found that the SFRM had sufficient bond strength to bear its self-weight, allowing the SFRM to keep its structural integrity in a fire. Kodur and Shakya (2013) found that elevated temperatures greatly affected the thermal properties of SFRMs. If the variation in thermal properties is not considered for SFRMs, an error of up to 40% could be obtained in predicting the fire resistance of protected steel members.

However, the production of gypsum and Portland cement contributes significantly to greenhouse gas emissions. The production of one tonne of Portland cement emits an average of 0.87 tonnes of carbon dioxide equivalent (CO_{2eq}), whereas the production of one tonne of calcined gypsum emits an average of 0.14 tonnes of CO_{2eq} (Fořt and Černý, 2018; McDonald et al., 2022). In Australia alone, the annual production of Portland cement is responsible for 7.4 million tonnes of emissions, producing about 1.3% of national emissions (Beyond Zero Emissions, 2017). On the other hand, Australian coal-fired power stations produce over 9.6 million tonnes of fly ash annually, but only about 46% of the annual production is effectively utilised within various civil and construction applications (Ash Development Association of Australia, 2022). The accumulated fly ash in Australia is estimated to be more than 400 million tonnes, posing a severe environmental problem (Beyond Zero Emissions, 2017). Because of the expected shutdown of the country's remaining coal-fired power stations, the annual production of fly ash in Australia is expected to decline gradually. However, the accumulated fly ash can still be used in a sensible way to tackle the global climate change crisis. Therefore, it would be favourable to develop sustainable SFRMs by fully or partially replacing gypsum and Portland cement with fly ash. No study has been reported in the literature on the use of fly ash as the major binder in SFRMs. It is worth noting that fly ash has been fully utilised in some countries (e.g., Italy and Netherlands) for different purposes. Care should be taken in evaluating the benefits of repurposing fly ash to make SFRMs in those countries.

Furthermore, lightweight and porous fillers (e.g. expanded vermiculite, expanded perlite, mica) are commonly used in SFRMs to reduce their thermal conductivity (Xie et al., 2020). However, these fillers are manufactured from natural and non-renewable minerals. In recent years, waste glass has been successfully upcycled and used to produce expanded glass granules, which have relatively high mechanical strength, high chemical resistance, and excellent heat resistance (softening point of around 700 °C) (Poraver, 2019). Expanded glass has been reported in the literature to produce lightweight concrete and aerated concrete blocks (Bumanis et al., 2013; Arslan and Celebi, 2019). But it also has low thermal conductivity due to the presence of a high volume of closed pores. It is postulated that expanded glass granules could be incorporated in SFRMs as thermal barriers to reduce the consumption of natural and non-renewable minerals, such as vermiculite and perlite. However, the effects of elevated temperatures on the thermal properties of SFRMs with expanded glass have not been reported in the literature. The understanding of the evolution of thermal properties at elevated temperatures is crucial for accurate prediction of the fire resistance of structural elements with SFRM protection.

Against the above background, this paper aims to study the feasibility of producing SFRMs using a large volume of fly ash (60% of the total weight of the binder) and incorporating expanded glass as a lightweight filler. The cost and carbon emissions of the binder in the Australian context will be further assessed and discussed. To meet the requirements of various applications, three SFRMs with different densities were developed in this study. The developed SFRMs were then characterised to study their various properties, including density, compressive strength, bond strength, non-combustibility, thermal conductivity, and specific heat. The overall structure of the study takes the form of four sections. Section 2 has attempted to describe the test program, including materials used, mix proportions, sample preparation, characterisation techniques, and test procedures. Section 3 discusses the test results and provides scientific explanations. Finally, Section 4 concludes the study by summarising the research findings.

This research will confirm the practicality of using fly ash and expanded glass in the development of SFRMs and highlight their benefits in reducing environmental impact and cost. The developed SFRMs exhibit excellent mechanical and thermal properties, which are comparable to those of commercially available SFRMs. It is expected that this research will contribute to the effective disposal of accumulated fly ash in Australia by commercialising the developed SFRMs.

Additionally, this paper will present the thermal properties of fly ash-based SFRMs at elevated temperatures, which have not been reported in the literature. This advanced knowledge and understanding of the thermal properties will allow the accurate prediction of fire resistance of structural elements using appropriate numerical and fire design methods. By incorporating this new knowledge into design, the fire safety of steel structures can be significantly enhanced at a lower cost. The transfer of this knowledge from research to practice will lead to a transformative change in construction practices, promoting the use of greener SFRMs.

Table 1
Specified properties of commercially available SFRMs.

Product	Binder	Density (kg/m^3)	Compressive strength (kPa)	Bond strength (kPa)	Thermal conductivity (W/m K)	Reference
A/D Type-5GP	Gypsum	240	177	9.5	0.086	A/D FIRE PROTECTION SYSTEMS (2017a)
CAFCO 300	Gypsum	240	158.5	19.4	0.078	ISOLATEK International (2018a)
Carboline Pyrolite 15	Gypsum	240	288	24.6	0.105	Carboline (2018)
Carboline Type-5MD	Gypsum	352	496	60.7	–	Carboline (2021)
Tyfo WR-AFP	Gypsum/cement	458	875.6	78.6	–	Aegion Corporation (2018)
Monokote MK-6s	Cement	240	71	16.9	–	gcp applied technologies (2019)
Blaze-Shield II	Cement	256	114	18	0.043	ISOLATEK International (2018c)
A/D Type-7GP	Cement	352	1840	95.8	–	A/D FIRE PROTECTION SYSTEMS (2017b)
CAFCO 400	Cement	405	1058.7	409.7	0.071	ISOLATEK International (2018b)
Fendolite M-II	Cement	706	3792.6	773.5	0.164	ISOLATEK International (2018d)

2. Experimental program

Three SFRMs with different densities were prepared and evaluated. This section presents details of the materials used and the preparation of the samples, followed by an overview of the experimental methods employed to measure the density, compressive strength, bond strength, non-combustibility, thermal conductivity, and specific heat. The experimental flowchart is illustrated in Fig. 1.

2.1. Materials

Four low-calcium fly ashes (Class F fly ash according to ASTM C618 (ASTM International, 2019a)) produced in Australia were tried to develop binders for SFRMs. The fly ashes were from four different sources: the Eraring power station in New South Wales (supplied by Boral); the Gladstone power station in Queensland (supplied by Cement Australia); the Callide power station in Queensland; and the Mt Piper power station in New South Wales. Commercially available ground granulated blast furnace slag (GGBS) was supplied by Australia Builders, and ordinary Portland cement (OPC) and hydrated lime were supplied by Cement Australia.

Expanded vermiculite and expanded perlite used as lightweight fillers were supplied by Ausperal Australia. Expanded glass granules made from post-consumer recycled glass were supplied by Poraver. Flame retardant expanded polystyrene (EPS) BST lightweight aggregates were supplied by Abrams Marketing. Commercially available polymer dispersion adhesive (polyvinyl acetate, PVA) was supplied by Selleys. White silica fume was supplied by Domcrete. Polypropylene (PP) fibres were supplied by Sika Australia, and alkali-resistant (AR) glass fibres were supplied by Hebei Yuniu Fibreglass Manufacturing, China.

Superplasticisers were used in the mix design to achieve reasonable strength, good workability and viscosity, and required sprayability. Based on our experimentation, superplasticisers BASF MasterGlenium SKY 8100 and MasterPolyheed 8820 were used in combination with BASF MasterPozzolith 80. In developing the low-density SFRM, BASF MasterAir 940 air-entraining admixture was used to increase the porosity and air content.

2.2. Mix proportions

GGBS (9%) and hydrated lime (12%) were added to the binder to promote the setting and early strength development of the high-volume (60%) fly ash blended cement (FAC). As can be seen, up to 81% of Portland cement was replaced by fly ash, GGBS, and hydrated lime in the binder. Various fillers (i.e., expanded vermiculite, expanded perlite, expanded glass, and BST lightweight aggregates) were included in the mixtures to develop SFRMs with different densities (low-density, medium-density, and high-density). Small amounts of PVA, silica fume and fibres were added to increase the strength of the SFRMs and their ability to bond to the substrate material, such as steel. The mix proportions of the SFRMs are given in Table 2.

2.3. Sample preparation

In preparing the SFRM mixtures, the lightweight fillers and FAC were first dry mixed for about 1 min in a pan mixer. Then water with dissolved PVA and other admixtures was added slowly to the mixture. The resulting mixing lasted for about 30 min until a homogenous mixture was obtained. The mixture was then transferred directly to a spray machine and sprayed onto galvanised steel plates or into moulds, as shown in Fig. 1.

2.4. Characterisation techniques

The chemical composition of various cementitious materials (e.g. fly

Table 2
Composition of SFRMs.

Composition (wt.%)	FAC-L	FAC-M	FAC-H
Blended cement (FAC)	51	51	53
Expanded vermiculite/perlite	26	20	40
Expanded glass	15	21	–
BST lightweight aggregate	<1	–	–
PVA	3	2	3
Silica fume	–	3	3
Fibres	–	<1	<1
Admixtures	4	2–3	<1

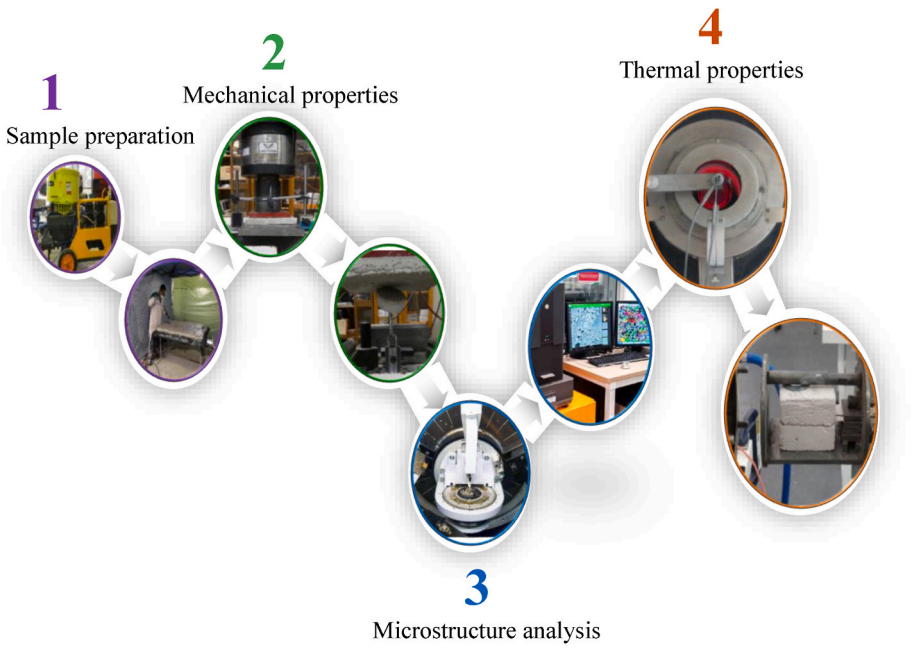

Fig. 1. Experimental flowchart for SFRM sample preparation and material characterisation.

ash, cement) was analysed using a JEOL JSM-6510 L V scanning electron microscope (SEM) equipped with an Amptek silicon drift detector (SDD) in order to perform energy dispersive spectroscopy (EDS). The particle size of fly ash was measured using a Thermo Fisher Scientific Phenom XL desktop SEM equipped with ParticleMetric analysis software in a low vacuum at an accelerating voltage of 15 keV. Powder X-ray diffraction (XRD) measurements were conducted on the raw cementitious materials and hardened pastes using a Bruker D8 Advance Diffractometer with CuKα radiation ($\lambda = 1.5406$ Å), LYNXEYE XE detector and Bragg-Brentano geometry. Surface area measurements were conducted on fly ashes using a Micromeritics ASAP 2020 system, and the Brunauer-Emmett-Teller (BET) method was used to calculate the surface areas.

Thermal analysis of SFRMs was performed using a Netzsch Jupiter 449C Simultaneous Thermal Analyser (STA), and Netzsch Proteus analysis software was used to draw and analyse the resulting thermogravimetry (TG) and differential scanning calorimetry (DSC) curves. Evolved gas analysis (EGA) was conducted on the hardened FAC paste. To conduct this analysis, the STA was connected by a heated transfer line to a Bruker Vertex 70 Fourier Transform Infrared (FTIR) spectrometer. Thermal strain measurements of SFRMs were conducted using a Netzsch 402 F1 Hyperion Thermo-Mechanical Analyser (TMA), and Netzsch Proteus analysis software was used to analyse the results. A cylindrical specimen approximately 9 mm in diameter and 28 mm in height was placed in an Al_2O_3 expansion/compression sample holder. The analyser was used to evaluate the dimension changes in the specimen at elevated temperatures (Kodur and Shakya, 2013).

Thermal conductivity and volumetric heat capacity of SFRMs were measured using a Hot Disk TPS 2500 S. A Kapton 5501 sensor with a pre-mounted room temperature cable for ambient temperature and a Mica 5082 sensor with a four-point probe macro sensor holder for higher temperatures up to 700 °C were used. It should be noted that this setup has a maximum use temperature of 750 °C. The heating power and measurement time utilised in the analysis were between 15 and 40 mW and 40–160 s, respectively.

2.5. Test procedures

The compressive strength of the FAC-based binder was measured using 50 mm cubic samples according to ASTM C109 (ASTM International, 2016). The cube specimens were demoulded after 24 h and kept in a humidity cabinet at a temperature of 23 °C and relative humidity of 50% before testing. Five specimens were tested at 3 or 28 days for each mix to measure the average strength.

To determine the density of SFRMs, tests were carried out according to ASTM E605 (ASTM International, 2019b). A thickness of approximately 20 mm SFRM was sprayed onto 400 × 400 × 1.5 mm galvanised steel plates using a spray machine. The samples were then conditioned for more than 72 h at room temperature and relative humidity of less than 60% until the weight readings differed by less than 1% within 24 h. A thickness gauge with a 29 mm diameter disc was used to measure the thickness of SFRMs. The displacement method was used to determine the density of SFRMs, where samples with dimensions of 85 × 85 × 20 mm (minimum sample size 131 cm^3) were cut and placed in a 1000 mL beaker filled with 1 mm unexpanded polystyrene beads. The bulk density was then calculated using the overflow volume and mass of the sample.

To determine the actual compressive strength of SFRMs applied to structural members, tests were carried out according to ASTM E761 (ASTM International, 2015). SFRM with a thickness of approximately 20 mm was applied to two 175 × 600 × 1.5 mm galvanised steel plates using a mortar spray machine. The samples were conditioned for 72 h at room temperature and relative humidity of less than 60%. After 72 h, the samples were forced-dried in an oven at 45 °C until a constant weight was reached. To measure the compressive strength, the load was applied perpendicular to the surface of the sample at two different points located at the opposite ends of the sample. The loading was applied to an area of 150 × 150 mm, which was capped with a layer of plaster (CSR Gyprock) with a thickness of up to 1.3 mm. An initial pressure of 0.7 kPa was applied to the sample, and then the load was increased at a loading speed of 1.3 mm/min. The sample was compressed until either deformation of 10% or the ultimate load was reached, whichever occurred first. Two linear variable differential transducers (LVDTs) were used to measure the deformation; one at the front and the other at the back.

To determine the cohesion/adhesion (bond strength) of SFRMs, tests were carried out according to ASTM E736 (ASTM International, 2019c). SFRM with a thickness of approximately 20 mm was applied to three 300 × 300 × 1.5 mm galvanised steel plates using a mortar spray machine. The samples were conditioned for 72 h at room temperature and a relative humidity of less than 60%. After 72 h, the samples were forced-dried in an oven at 45 °C until a constant weight was reached with a difference of less than 1%. Plastic caps were bonded to the surface of the SFRM using Sika adhesive. The samples were then attached to the testing machine with the SFRM facing down. A uniform tensile load at a loading rate of 49 N/min (5 kg/min) was applied to pull the plastic cap. The force at the time of failure was recorded accordingly.

The non-combustibility of SFRMs was evaluated using a tube furnace with a cone-shaped airflow stabiliser in accordance with the test procedures specified in AS 1530.1 (Standards Australia, 2016). Five cylindrical samples with a height of 50 mm and a diameter of 45 mm were prepared. A 2-mm diameter hole was made axially from the geometric centre of the top of the specimen to install the centre thermocouple. The samples were conditioned in an oven at 60 °C for 24 h and then cooled to ambient temperature in a desiccator prior to testing. The mass of each sample was measured to an accuracy of 0.1 g prior to testing in the furnace. In order to evaluate the non-combustibility, three K-type thermocouples were used to measure the temperature change of the sample, which were placed on the furnace wall (T-furnace), the sample surface (T-surface), and the sample centre (T-centre), respectively. Prior to the testing, the furnace temperature was stabilised at 750 ± 5 °C without the inserted specimen and the specimen holder for at least 10 min with a drift of not more than 2 °C in 10 min.

After the furnace temperature was stabilised, a specimen along with its holder was inserted into the furnace from the top. The initial, maximum and final temperatures at different locations were measured by the furnace thermocouple and two other sample thermocouples. During the testing, any occurrence and duration of flames of the sample were recorded. After 30 min, when all three thermocouples reached temperature equilibrium (the temperature change measured by a thermocouple was within 2 °C over a period of 10 min), the test was terminated. If the equilibrium was not reached at 30 min, the test would continue until all three thermocouples had reached temperature equilibrium, as specified in AS 1530.1 (Standards Australia, 2016). After the test, the sample was taken out of the furnace and cooled to ambient temperature, and then the residual mass of the sample was weighed.

3. Results and discussion

This section reports the characterisation results of the raw materials and the mechanical and thermal properties of the developed FAC binders and SFRMs. The research findings will be discussed based on the microstructure analysis. Meanwhile, an environmental and cost analysis will be presented to justify the benefits of the developed FAC binders.

3.1. Raw materials

The oxide compositions of the raw materials (i.e., GGBS, OPC, and hydrated lime) are shown in Table 3. Calcium is the main element in the GGBS, OPC and hydrated lime. Silicon and aluminium are also abundant in the GGBS and OPC. XRD analysis was performed to identify the phases in the raw materials, and the results are shown in Fig. 2. Amorphous phases and gypsum ($CaSO_4{\cdot}2H_2O$, PDF# 70–0982) are the main phases in the GGBS. Tricalcium silicate (Ca_3SiO_5, PDF# 02–0849), dicalcium

Table 3
Chemical compositions of raw materials (% by total mass).

Material	Al_2O_3	SiO_2	CaO	Fe_2O_3	K_2O	MgO	Na_2O	SO_3	TiO_2	MnO	LOI
GGBS	13.8	32.1	41.7	0.6	0.3	5.0	<0.1	5.3	0.8	0.3	1.2
Portland cement	6.6	20.8	60.8	3.6	0.4	1.6	0.6	5.0	0.4	–	3.9
Hydrated lime	–	1.6	98.4	–	–	–	–	–	–	–	24.0

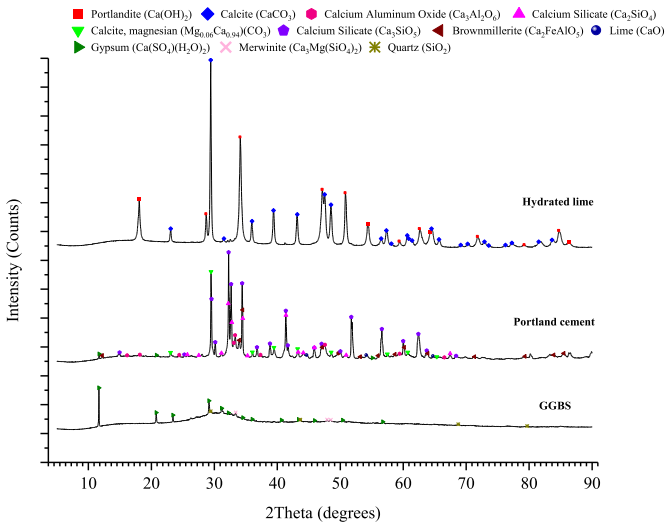

Fig. 2. XRD diffractograms of raw materials: hydrated lime, Portland cement, and GGBS.

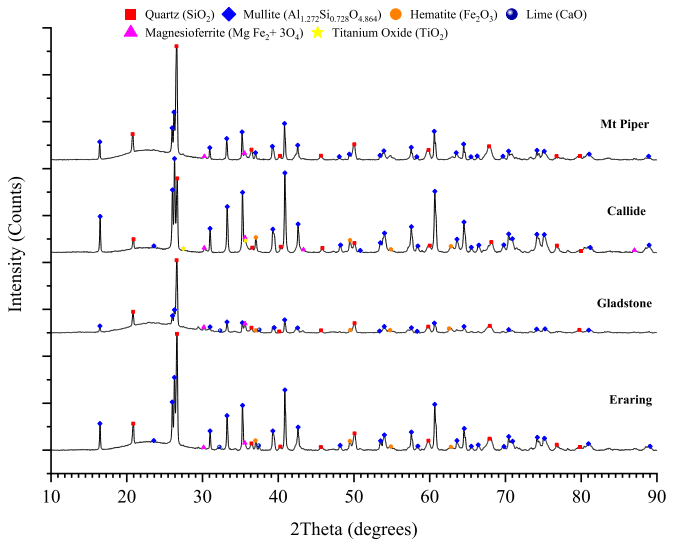

Fig. 3. XRD diffractograms of fly ashes: Mt Piper, Callide, Gladstone, and Eraring.

silicate (Ca_2SiO_4, PDF# 49–1672), calcite ($(Mg_{0.06}Ca_{0.94})(CO_3)$, PDF# 83–0578), and brownmillerite (Ca_2FeAlO_5, PDF# 70–2764) are the main crystalline phases in the Portland cement. Portlandite ($Ca(OH)_2$, PDF# 76–0571) and calcite ($CaCO_3$, PDF# 86–2335) are the main crystalline phases in the hydrated lime.

The low-calcium Class F fly ashes collected from the four different power plants (Eraring, Gladstone, Callide, and Mt Piper) in Australia were characterised before they were used to produce FAC binders in the laboratory. The chemical compositions of the fly ashes are shown in Table 4. As expected, silicon is the main element of fly ashes, followed by aluminium and iron. The Mt Piper fly ash has the highest silicon content, the Callide fly ash has the highest aluminium and iron contents, and the Gladstone fly ash has the highest calcium content. The XRD diffractograms in Fig. 3 show that mullite ($Al_{1.272}Si_{0.728}O_{4.864}$, PDF# 06–0259), quartz (SiO_2, PDF# 05–0490), and hematite (Fe_2O_3, PDF# 13–0534) are the main crystalline phases in the fly ashes. Compared with other fly ashes, the Gladstone fly ash has the least mullite content.

Table 5 shows the BET surface area, total pore volume, average particle size, and medium particle size of each fly ash. The measured BET surface areas of the four fly ashes range from 1.30 to 2.26 m^2/g, whereas the average and medium particle sizes of the fly ashes range from 7.65 to 10.30 μm and 7.07–9.18 μm, respectively. While the Eraring and Gladstone fly ashes have relatively large BET surface areas, the Callide and Mt Piper fly ashes have much smaller BET surface areas because of their relatively low total pore volumes and large particle sizes. Fig. 4 shows the SEM backscattered electrons (BSE) images of the fly ashes.

Table 5
Properties of fly ashes.

	Eraring	Gladstone	Callide	Mt Piper
BET surface area (m^2/g)	2.1857 ± 0.0027	2.2644 ± 0.0020	1.8642 ± 0.0020	1.3027 ± 0.0015
Total pore volume (cm^3/g)	0.001830	0.002310	0.000814	0.000599
Average diameter (μm)	9.77	7.65	10.30	9.92
Medium diameter (μm)	8.81	7.07	9.18	8.53

The Gladstone fly ash has the smallest average particle size, followed by the Eraring and Mt Piper fly ashes. The Callide fly ash has the largest average particle size.

3.2. FAC binders

3.2.1. Compressive strengths

The four fly ashes were used to make FAC binders with a constant water-to-binder ratio of 0.25. The obtained compressive strengths at 3 and 28 days are compared in Fig. 5. The FAC binder made from the Gladstone fly ash achieved the highest compressive strength of 46.3 MPa at 28 days, and the binder made from the Callide fly ash achieved a similar but slightly lower compressive strength. Among the four fly

Table 4
Chemical compositions of fly ashes (% by total mass).

Material	Al_2O_3	SiO_2	CaO	Fe_2O_3	K_2O	MgO	Na_2O	SO_3	TiO_2	LOI
Eraring	26.5	63.4	2.5	3.0	1.5	1.4	0.9	<0.1	1.0	1.2
Gladstone	22.9	63.5	2.7	5.4	1.4	2.2	1.0	<0.1	0.8	1.0
Callide	33.4	53.0	1.3	7.5	0.3	1.2	0.2	<0.1	3.1	0.3
Mt Piper	22.8	69.2	<0.1	2.0	2.5	0.8	0.8	0.7	1.2	2.2

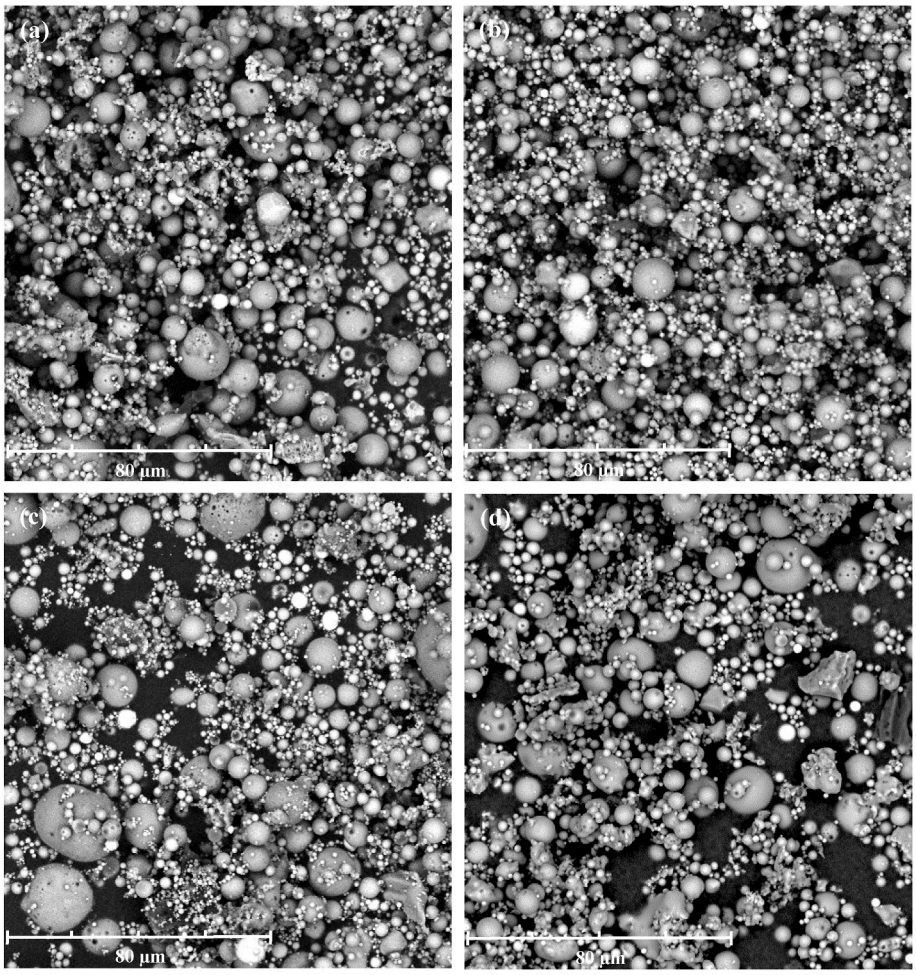

Fig. 4. SEM-BSE images of fly ashes: (a) Eraring, (b) Gladstone, (c) Callide, and (d) Mt Piper.

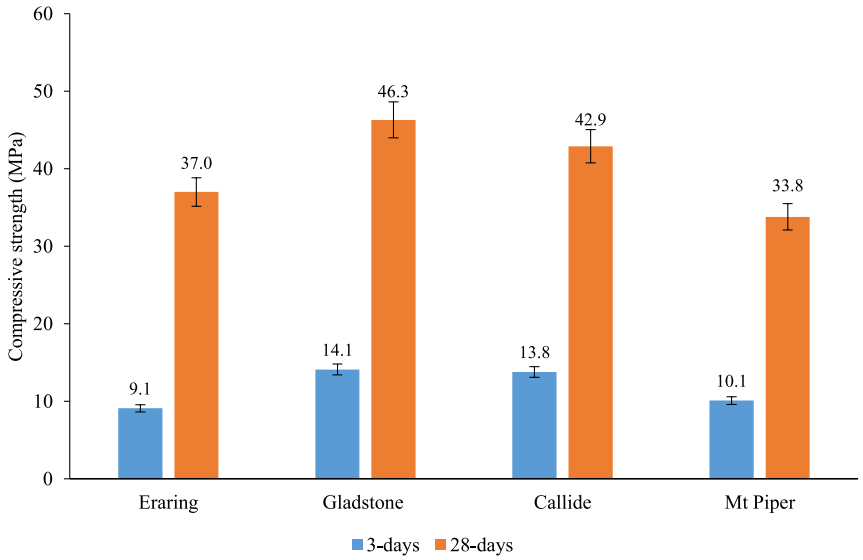

Fig. 5. Compressive strengths of FAC binders using Eraring, Gladstone, Callide, and Mt Piper fly ashes.

ashes, the Mt Piper fly ash was the only one that produced a binder with a 28-day compressive strength (33.8 MPa) slightly lower than the suggested strength of 35 MPa for binders, according to AS 3972 (Standards Australia, 2010).

Leong et al. (2016) reported that the chemical composition, mineralogy, and particle size of fly ash had a significant influence on the

compressive strength of developed binders. The measurement results in Table 5 showed that the Gladstone fly ash had the largest BET surface area and the smallest average particle size among the four fly ashes. Thus, the high compressive strength achieved from the Gladstone fly ash in this study can be explained by its high surface area and small particle size (Gunasekara et al., 2017; Sweeney et al., 2017). Meanwhile, Sweeney et al. (2017) and Gunasekara et al. (2017) also reported that the Gladstone fly ash has a nearly ideal reactive Si/Al ratio of 2.0–2.4 for making geopolymers. They found that the geopolymers made with Gladstone fly ash achieved the best mechanical properties compared to geopolymers made with fly ashes from other sources. Although this study used fly ash to develop FAC binders rather than geopolymers, it can be postulated that the pozzolanic reaction between fly ash and calcium hydroxide in a FAC binder has also been affected by the physical properties and chemical composition of the fly ash.

As Gladstone fly ash has been widely used by Australian researchers in making various construction materials, this type of fly ash was selected in the following study to make the FAC binder for SFRM. Nonetheless, it should be noted that other low-calcium fly ashes produced in Australia should also be suitable for producing FAC binders, as strength requirements on SFRMs are relatively low (<4 MPa). Towards future commercial production of SFRM, local fly ash available near the production site should be adopted to minimise the transportation distance.

3.2.2. X-ray diffraction

The XRD diffractograms are shown in Fig. 6 for the FAC binder made from the Gladstone fly ash after exposure to 20 °C, 100 °C, 200 °C, 400 °C, 600 °C, 800 °C and 1000 °C, respectively. The XRD diffractogram of the FAC binder at 20 °C shows that portlandite ($Ca(OH)_2$, PDF# 72–0156), aluminium tobermorite ($Ca_5Si_5Al(OH)O_{17}{\cdot}5H_2O$, PDF# 19–0052), gypsum ($CaSO_4{\cdot}2H_2O$, PDF# 06–0046) and calcium aluminium oxide sulphite hydrate ($Ca_6Al_2O_6(SO_3)_3{\cdot}32H_2O$, PDF# 41–0217) are the main hydration phases. The hydration process of the FAC binder is generally similar to that of OPC. But some new phases, such as aluminium tobermorite and gibbsite ($Al(OH)_3$, PDF# 07–0324), were detected in the FAC binder due to the inclusion of fly ash, GGBS, and hydrated lime (Hewlett and Liska, 2017). At 200 °C, gypsum, calcium aluminium oxide sulphite hydrate, and calcium aluminium oxide nitrate hydrate ($Ca_4Al_2O_6(NO_3)_2{\cdot}8H_2O$, PDF# 54–0850) disappeared due to thermal dehydration. Meanwhile, in the temperature range of 20–400 °C, there was a drop in the intensities of portlandite, gibbsite and aluminium tobermorite reflections with increasing temperature, which was associated with increased thermal and structural disorder due to dehydration (Rodriguez et al., 2017). At 600 °C, portlandite, gibbsite, and aluminium tobermorite disappeared, indicating that the decomposition occurred between 400 and 600 °C. At 800 °C, dolomite ($CaMg(CO_3)_2$, PDF# 79–1343) and calcite ($(Mg_{0.06}Ca_{0.94})(CO_3)$, PDF# 86–2335) disappeared along with the increase in the peak intensity of lime (CaO, PDF# 03–7161), indicating complete decarbonisation. At this temperature, the formation of dicalcium silicate (Ca_2SiO_4, PDF# 33–0303) was also observed. At 1000 °C, dicalcium silicate disappeared, but the formation of tricalcium aluminate ($Ca_3Al_2O_6$, PDF# 32–0150), anorthite ($CaAl_2Si_2O_8$, PDF# 41–1486), gehlenite ($Ca_2Mg_{0.08}Al_{1.84}Si_{1.08}O_7$, PDF# 14–4684), calcium iron oxide ($Ca_4Fe_9O_{17}$, PDF# 21–0913), wollastonite-1A ($(Ca_{2.87}Fe_{0.13})(SiO_3)_3$, PDF# 83–2198), and grossular ($Ca_3(Al_{1.332}Fe_{0.668})(SiO_4)_3$, PDF# 85–1369) was observed. It has been reported that anorthite, gehlenite, and wollastonite-1A could form from tricalcium aluminate and dicalcium silicate at temperatures above 800 °C, with grossular as an intermediate product (Doval et al., 2006; Kotsis and Balogh, 1989). When the temperature increased from 900 °C to 1060 °C, grossular decomposed into anorthite, gehlenite, and wollastonite-1A via a solid-state decomposition (grossular → anorthite + gehlenite + wollastonite) (Yoder Jr, 1950).

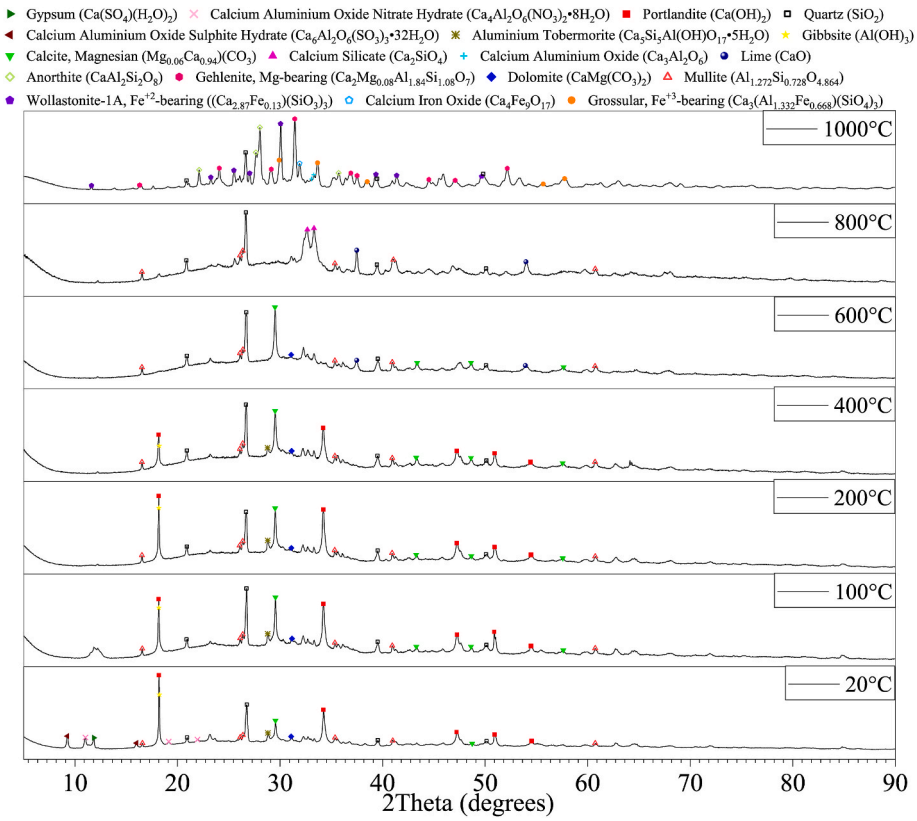

Fig. 6. XRD diffractograms of FAC binder at 20 °C, 100 °C, 200 °C, 400 °C, 600 °C, 800 °C, and 1000 °C.

3.2.3. Simultaneous thermal analysis

The TG and DSC thermograms of the FAC binder are shown in Fig. 7. It should be noted that an upward peak in the DSC curve indicates an exothermic reaction, whereas a downward peak represents an endothermic reaction. The first two endothermic peaks occurred at 90.7 °C and 137.4 °C, respectively. They were due to dehydration reactions, where water was released during the dehydration of calcium aluminate-based hydrates, gypsum, and hemihydrate (Sha and Pereira, 2001; Strydom et al., 1995). This is supported by the XRD results in Fig. 6, indicating that the peaks for gypsum, calcium aluminium oxide sulphite hydrate, and calcium aluminium oxide nitrate hydrate disappeared when the temperature increased from 100 °C to 200 °C. The third major endothermic peak occurred at 441.6 °C corresponds to the dehydration of portlandite (Zhang and Ye, 2012). The following two endothermic peaks occurred at 704.7 °C and 726.9 °C corresponding to the decarbonisation of dolomite and calcite, respectively, which was confirmed by the XRD analysis. The decarbonisation of dolomite occurred earlier than that of calcite (Valverde et al., 2015). The following two exothermic peaks occurred at 915.5 °C and 1021.7 °C, respectively. In this temperature range, no obvious mass loss was observed in the TG curve. This indicates that the exothermic peaks were associated with solid-solid phase transformations. These exothermal events might correspond to the transformation of dicalcium silicate into gehlenite and wollastonite-β (Majerová et al., 2020; Rodriguez et al., 2017), and the presence of gehlenite and wollastonite has been demonstrated by the X-ray analysis. It was reported that gehlenite crystallised at 850 °C, and wollastonite-β formed in the temperature range of 950–1050 °C (Bernardo et al., 2009).

3.2.4. Evolved gas analysis

The coupled STA-FTIR is an effective tool for evaluating gaseous products produced during thermal degradation, particularly the release of H_2O and CO_2 from cementitious phases under thermal treatment (Rodriguez et al., 2017). The three-dimensional (3D) FTIR spectra of the FAC binder are shown in Fig. 8. The peaks at the wavelengths of 1330–1730 cm^{-1} and 3530−3915 cm^{-1} were corresponding to H_2O, whereas the peaks at the wavelengths of 600–680 cm^{-1} and 2290−2390 cm^{-1} were attributed to CO_2 (Han et al., 2022). The release of H_2O corresponds to the dehydration of calcium aluminate hydrates (because of the reaction between hydrated lime and GGBS) and gypsum (presented in the GGBS) at lower temperatures and the dehydration of portlandite at higher temperatures. The dehydration of calcium aluminate hydrates and gypsum finished at around 150 °C, and the dehydration of portlandite finished at around 470 °C. The release of CO_2 corresponds to the decarbonisation of dolomite and calcite, and the reaction finished at about 810 °C. These results are consistent with the XRD, TG and DSC results.

3.2.5. Environmental and cost analysis of binders

The authors recently developed carbonate-activated hybrid cement, and an environmental and cost analysis was carried out to justify its benefits (Huang et al., 2022). A similar analysis was conducted in this study for the developed FAC binder, where the total greenhouse gas emissions (GHG_{Total}) were computed to evaluate the environmental impact of the FAC binder in accordance with Eq. (1). It should be noted that the analysis followed the same well-established procedure described by Maddalena et al. (2018) and McLellan et al. (2011).

$$GHG_{Total} = \sum_{i=1}^{n} m_i(d_i e_i + p_i) \quad (1)$$

where n is the total number of ingredients used in the binder; m_i and d_i are the mass and transportation distance of the ingredient i, respectively; e_i is the emission factor, which was taken as 0.09 $kgCO_{2\text{-eq}}$/(km tonne) for road transport in Australia (Maddalena et al., 2018); and p_i is the emission per unit mass of the ingredient i from the production process. The p_i-values and transport distances (d_i) of fly ash, Portland cement, and GGBS used by Huang et al. (2022) were also used in this study. The p_i-value of hydrated lime was taken as 683 $kgCO_{2\text{-eq}}$/tonne (Shan et al., 2016), and its transport distance (84 km) was the same as that taken for Portland cement.

The calculated GHG_{Total} from Eq. (1) is 252 $kgCO_{2\text{-eq}}$/tonne for the developed FAC binder. In contrast, the typical value of GHG_{Total} is 798 $kgCO_{2\text{-eq}}$/tonne for Portland cement in Australia (O'Brien et al., 2009; Huang et al., 2022). Therefore, using the FAC binder to replace Portland cement can reduce carbon emissions by 68.4%, which demonstrates the significant environmental benefits of using the FAC binder to make SFRM.

A cost analysis was also conducted for the FAC binder to determine the overall cost (C_t) using Eq. (2) (Ma et al., 2018; Huang et al., 2022):

$$C_t = \sum_{i=1}^{n}(m_i \times C_i) \quad (2)$$

where C_i is the unit price of the ingredient i in the binder. Based on recent quotations and survey data, unit prices of Portland cement, GGBS, fly ash, and hydrated lime in Australia were taken as AU$372, AU$300, AU$180, and AU$192 per tonne, respectively. It is worth noting that the material prices used herein are wholesale prices for conducting a meaningful cost analysis, following the same approach adopted by

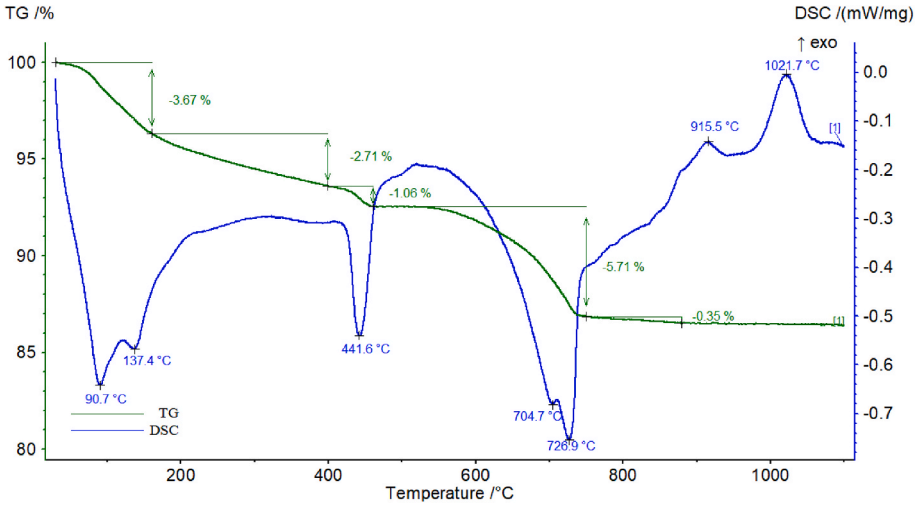

Fig. 7. TG and DSC thermograms of FAC binder after 28 days.

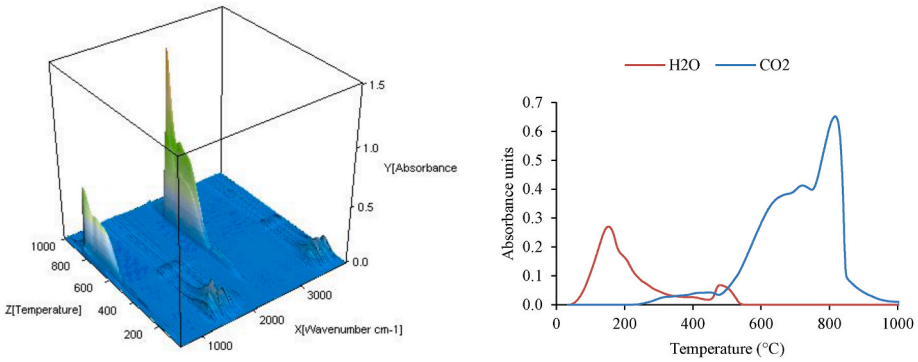

Fig. 8. 3D surface plot for STA-FTIR spectra of the evolved gaseous products by FAC binder (left), and the gases produced from FAC binder (right).

others (McLellan et al., 2011; Ma et al., 2018).

The calculated cost of the FAC binder from Eq. (2) is AU$229 per tonne. Compared with the unit price (AU$372 per tonne) of Portland cement in Australia, the material cost of the FAC binder is 38.4% lower. It should be noted that the cost analysis was based on the assumption of a typical transport distance of 129 km for fly ash (McLellan et al., 2011). The production of FAC binders might be less cost-effective if a longer transport distance is required for fly ash. A cost sensitivity analysis was conducted by increasing the transport distance of fly ash following the same procedure described by O'Brien et al. (2009) and Huang et al. (2022). It is assumed that the production of FAC binders is in Brisbane, Queensland, and fly ash needs to be transported from Stanwell Power Station to Brisbane. In this scenario, the transport distance is 654 km, which is relatively long. Based on the peak diesel price of AU$2.418 per litre in the last 12 months, the material cost of the FAC binder will be increased to AU$251 per tonne. But it is still 32.5% cheaper than that (AU$372 per tonne) of Portland cement. Thus, it can be concluded that it is more cost-effective to manufacture SFRM in Australia using FAC binder instead of Portland cement.

Considering the price volatility, the cost analysis will be less accurate with elapsed time. Nonetheless, it will not change the conclusion of the cost analysis in the foreseeable future. As the cost analysis was specially conducted for making FAC binders in Australia, the results of the cost analysis may not be relevant to some other countries or regions.

3.3. SFRMs

3.3.1. Room-temperature density and mechanical properties

For low-, medium-, and high-density SFRMs, there are minimum requirements for their compressive strengths and bond strengths measured at ambient temperature, as presented in Table 6. In this study, three SFRMs (FAC-L, FAC-M, and FAC-H) were developed, which could be classified as low-, medium-, and high-density SFRMs, respectively. Fig. 9 shows the developed SFRMs. As expected, the FAC-L samples exhibited higher porosity than the FAC-M and FAC-H samples due to the incorporation of a higher amount of lightweight fillers in the former. Table 6 shows the measured room temperature density, compressive strength, and bond strength of each SFRM. The measurement error of density was very small (≤2.1%). Therefore, the average value of three measurements is presented in Table 6 for the density of a SFRM. In contrast, the measured compressive strength and bond strength of a SFRM showed considerable variation between samples. Accordingly, the measured compressive strength or bond strength is shown as a range. For example, the measured compressive strength of FAC-L is in the range of 747–888 kPa.

As can be seen in Table 6, the density of a developed SFRM is within the specified range of the corresponding density group. Meanwhile, the compressive and bond strengths are also higher than the specified minimum values. It is worth noting that the compressive strengths of low-density FAC-L and medium-density FAC-M are much higher than the corresponding minimum required compressive strengths. This is due to the use of high-strength expanded glass granules in the two mixtures (Poraver, 2019). In contrast, the compressive strength of FAC-H without expanded glass was only about half that of FAC-M. It was also found that the bond strength of a SFRM had a direct correlation with its density. In general, the bond strength decreased with decreasing density.

Table 1 lists the specified densities, compressive strengths, and bond strengths of seven low-density, two medium-density and one high-density SFRMs; all these SFRMs are commercial products. For low-density SFRMs in Table 1, the specified compressive strength varies from 71 kPa to 1840 kPa, and the specified bond strength varies from 9.5 kPa to 95.8 kPa. The large variations in compressive strength and bond strength are due to variations in the type and content of binders and lightweight fillers. It can be argued that the developed FAC-L in this study has comparable compressive strength (747−888 kPa) and bond strength (14.4−19.3 kPa) to commercial products. For the two medium-density SFRMs in Table 1, Tyfo WR-AFP is a gypsum/cement-based SFRM, and CAFCO 400 is a Portland cement-based SFRM. Their specified compressive strengths are 875.6 kPa and 1058.7 kPa, respectively, which are much lower than the compressive strength (6188–7314 kPa) of the developed FAC-M in this study. The specified bond strengths of the two commercial products are 78.6 kPa and 409.7 kPa, respectively, which are higher than the bond strength (34.0–40.9 kPa) of FAC-M. This is because the FAC binder used in FAC-M had a large volume of fly ash and very little Portland cement. For the high-density SFRM in Table 1, the Portland cement-based SFRM Fendolite M-II has a specified compressive strength of 3792.6 kPa and a specified bond strength of 773.5 kPa (ISOLATEK International, 2018d). In contrast, the developed FAC-H in this study had a lower compressive strength (2343−3535 kPa) and a lower bond strength (51.5−85.1 kPa). Once again, this is due to the use of the FAC binder in FAC-H.

Table 6
Physical and mechanical properties of SFRMs.

SFRM	Low density[a]	FAC-L	Medium density[a]	FAC-M	High density[a]	FAC-H
Average density (kg/m^3)	240–352	345	353–640	560	641–750	698
Compressive strength (kPa)	Min 68.9	747–888	Min 351.7	6188−7314	Min 2068	2343−3535
Bond strength (kPa)	Min 7.2	14.4–19.3	Min 20.6	34.0–40.9	Min 47.9	51.5–85.1

[a] Recommended performance (ISOLATEK International, 2019; MasterFormat, 2011).

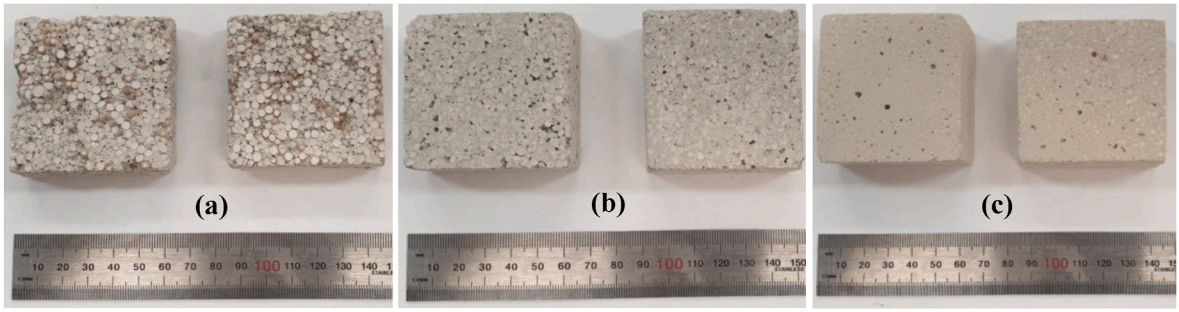

Fig. 9. Photographs of developed SFRMs: (a) FAC-L, (b) FAC-M, and (c) FAC-H.

3.3.2. Non-combustibility

To protect structures from a fire, SFRM itself is preferred to be non-combustible. Both AS 1530.1 (Standards Australia, 2016) and ASTM E2652 (ASTM International, 2018) suggest a similar procedure for the combustibility test, but different criteria are adopted by them in determining combustibility, as summarised in Table 7. According to AS 1530.1 (Clause 3.4), a material is considered combustible under any of the following circumstances: (a) sustained flaming for 5s or longer (disregards any individual flaming less than 5 s); (b) the average furnace temperature rise exceeds 50 °C; and (c) the average specimen surface temperature rise exceeds 50 °C. In contrast, ASTM E2652 classifies a material as combustible under any of the following circumstances: (a) the duration of sustained flaming exceeds 10 s; (b) the average furnace temperature rise exceeds 30 °C; (c) the average specimen surface temperature rise exceeds 30 °C; and (d) the average weight loss of the tested specimens exceeds 50%. Compared with ASTM E2652, AS 1530.1 is more stringent in terms of the time duration of sustained flaming but less stringent in terms of temperature rise. Meanwhile, ASTM E2652 has an additional requirement for weight loss.

Table 7 presents the combustibility test results of the three developed SFRMs. The maximum average furnace temperature rise of 10.0 °C was found in FAC-H, whereas the maximum average specimen surface temperature rise of 9.0 °C was found in FAC-L. Both temperature rises were less than the specified limits of 30 °C in ASTM E2652 or 50 °C in AS 1530.1. In terms of temperature rises in the centre of a test specimen, FAC-M had the lowest temperature rise of 18.1 °C because it contained the least amount of combustible ingredients. In contrast, FAC-L had the highest temperature rise of 37.9 °C mainly because of the inclusion of about 1 wt% BST aggregate. Although the BST aggregate was flame-retardant, it could melt and decompose when exposed to temperatures above 490 °C (Ramli Sulong et al., 2019). However, as the amount of BST lightweight aggregates was very little in FAC-L, its central temperature rise (37.9 °C) was relatively small, and the duration of sustained flaming only lasted for 2–3 s. Furthermore, the weight loss of all tested samples was within 10%, which is much less than the specified limit of 50% (ASTM International, 2018). It can be concluded that all three SFRMs can be classified as non-combustible according to either AS 1530.1 or ASTM E2652.

Table 7
Non-combustibility test results of SFRMs.

SFRM	AS 1530.1 (2016)	ASTM E2652 (2018)	FAC-L	FAC-M	FAC-H
Mass loss	–	≤50%	9.9%	8.0%	9.9%
Total duration of sustained flaming	<5 s	<10 s	2–3 s[a]	Nil	Nil
Furnace thermocouple temperature rise	≤50 °C	≤30 °C	4.7 °C	7.3 °C	10.0 °C
Specimen centre thermocouple temperature rise	–	–	37.9 °C	18.1 °C	25.6 °C
Specimen surface thermocouple temperature rise	≤50 °C	≤30 °C	9.0 °C	4.6 °C	8.0 °C

[a] Disregards any individual duration of flaming less than 5 s according to AS 1530.1.

3.3.3. Thermogravimetric analysis

The mass losses as a function of temperature are shown in Fig. 10 for the three developed SFRMs. Due to the evaporation of free water, a small mass loss was observed at the beginning of the heating process up to 100 °C. Then a significant mass loss was found in the temperature range of 100–200 °C due to the fast evaporation of free water. Further mass loss at a lower rate occurred in the temperature range of 200–700 °C, which was mainly attributed to the release of chemically bound water present in the SFRMs. In the temperature range of 700–800 °C, a quick drop in mass was observed, which was attributed to the decarbonisation of dolomite and calcite (Valverde et al., 2015; Rodriguez et al., 2017). Beyond 800 °C, the mass of a developed SFRM remained relatively stable. Compared to FAC-L, FAC-M and FAC-H exhibited higher mass loss mainly because of their higher moisture contents. The moisture content of FAC-L was 2.8% at the time of testing, whereas those of FAC-M and FAC-H were 4.6% and 4.5%, respectively. At 1000 °C, the total mass losses of FAC-L, FAC-M and FAC-H were 11.4%, 14.1% and 14.5%, respectively. It should be noted that the mass loss tests were repeated on two identical specimens, and the discrepancy between measured values at the same temperature was within 5%.

Carino et al. (2005) and Kodur and Shakya (2013) measured mass losses of four commercially available SFRMs (i.e., CAFCO 300, Carboline Type-5MD, Tyfo WR-AFP, and Blaze-Shield II), and the results are presented in Fig. 10. Compared with the commercial products, the

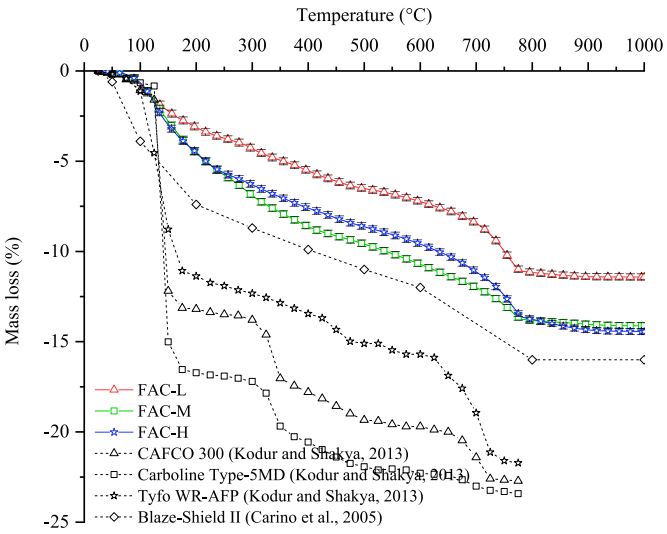

Fig. 10. Mass loss as a function of temperature.

developed SFRMs in this study generally had lower mass losses. When the temperatures were the same, the mass loss of the cement-based Blaze-Shield II was slightly higher than those of the developed SFRMs in this study, which could be attributed to the higher moisture content in Blaze-Shield II. The gypsum-based CAFCO 300 and Carboline Type-5MD had the highest mass losses among all SFRMs, followed by Tyfo WR-AFP with a mixture of gypsum and cement. In the temperature range of 100–180 °C, the rapid mass losses observed in these SFRMs containing gypsum ($CaSO_4{\cdot}2H_2O$) were due to dehydration. At 350 °C, a sudden drop in mass loss was reported for both CAFCO 300 and Carboline Type-5MD, which was attributable to the increased gypsum crystallisation (Kodur and Shakya, 2013). This phenomenon was not observed in Tyfo WR-AFP due to the lower gypsum content.

3.3.4. Thermal contraction/expansion

The measured thermal strains of the developed SFRMs are shown in Fig. 11 as a function of temperature. All SFRMs in this study exhibited thermal shrinkage. In the temperature range of 100–500 °C, the thermal shrinkage was due to the loss of free and chemically bound water in the SFRMs. Compared to FAC-H, the other two SFRMs (i.e., FAC-L and FAC-M) demonstrated smaller thermal contraction at a temperature below 600 °C. This could be due to the compensation effect of thermal expansion of the expanded glass (15% in FAC-L and 21% in FAC-M) in the two SFRMs. When heated from 20 °C to 300 °C, the thermal expansion coefficient of soda-lime glass increases from 8.6×10^{-6} °C^{-1} to 11.9×10^{-6} °C^{-1} (Carvill, 1993). In the temperature range of 500–800 °C, the contraction rates of all three SFRMs significantly increased, which was mainly due to the chemical decomposition of dolomite and calcite in the binder. It is worth noting that the thermal contraction of FAC-L and FAC-M exceeded that of FAC-H at above 800 °C. This could be explained by the softening of expanded glass at around 700 °C (Aslani and Ma, 2018; Poraver, 2019), which might lead to pore collapse in the expanded glass.

At below 600 °C, the thermal strains of the SFRMs developed in this study were comparable to those of the commercial products. In the range of 600–800 °C, however, the commercial SFRMs had relatively stable thermal strains, which could be due to the inclusion of a large amount of vermiculite to compensate for high-temperature shrinkage. In particular, CAFCO 300 with about 35% vermiculite even exhibited an obvious thermal expansion (Kodur and Shakya, 2013). Although the SFRMs developed in this study exhibited higher shrinkage than the commercial SFRMs in the range of 600–800 °C, the thermal strains of the former stabilised at around 800 °C. However, the thermal strains of the commercial products increased significantly beyond 800 °C.

3.3.5. Density at elevated temperatures

It is difficult to directly measure the density of a SFRM at elevated temperatures. Therefore, two indirect methods were adopted in this study. Following the method adopted by Kodur and Shakya (2013), Method I replaced the high-temperature density with the room-temperature density directly measured from specimens after exposure to the same high temperature. In the hot disk experiments, the specimens were removed from the furnace and then cooled to ambient temperature before conducting the measurements. This method ignored any mass or volume changes during the cooling process. Method II calculated the high-temperature density based on the thermogravimetric analysis (TGA) and thermomechanical analysis (TMA) for thermal contraction/expansion measurements described in Sections 3.3.3 and 3.3.4, respectively. This method was adopted by Carino et al. (2005) and Bentz and Prasad (2007), where the mass change was determined by TGA, and the volume change was determined by TMA. It should be noted that the material was assumed to be isotropic when determining the volume change.

The measured densities of the three SFRMs at elevated temperatures are shown in Fig. 12. In general, the obtained densities from the two methods were very close, and the maximum difference between them was within 2%. From a practical standpoint, Method I is usually sufficient for the measurement of high-temperature density. As can be seen in Fig. 12, the density of a SFRM decreased with increasing temperature. At 700 °C, the density decrease ranged from 8.9% to 10.3% with respect to the room-temperature density. The decrease in density was mainly due to dehydration and decarbonisation of the SFRM binder. In contrast, the three commercially available SFRMs CAFCO 300, Carboline Type-5MD, and Tyfo WR-AFP were reported to have a density reduction of 15–19% at 700 °C (Kodur and Shakya, 2013). The developed SFRMs in this study showed a lower density decrease compared to the commercially available SFRMs.

3.3.6. Thermal conductivity

The thermal conductivity (k) of a SFRM is shown in Fig. 13 as a function of temperature. At ambient temperature, the k-value increases with increasing density. The increased thermal conductivity of the SFRM with a higher density is associated with its less porous microstructure. For the high-density SFRM (FAC-H), k decreased with increasing temperature in the temperature range of 100–300 °C, which was due to the water evaporation (Ma et al., 2019). This is consistent with the test results of the commercial high-density SFRM (Tyfo WR-AFP) reported by Ma et al. (2019). However, this phenomenon was not observed in the

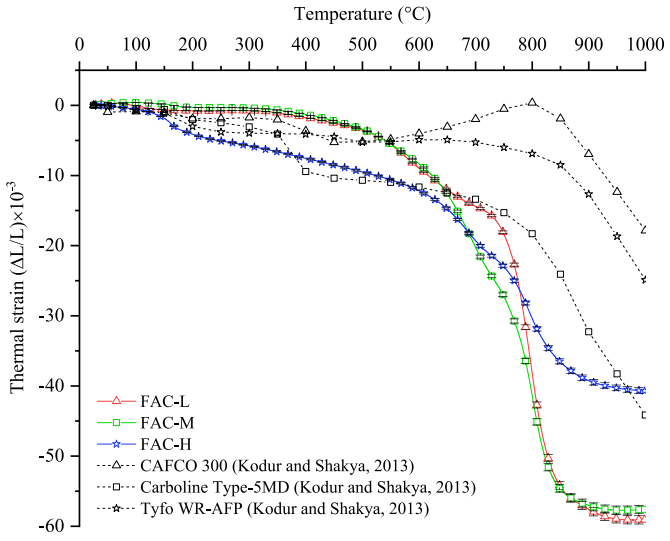

Fig. 11. Thermal shrinkage/expansion as a function of temperature.

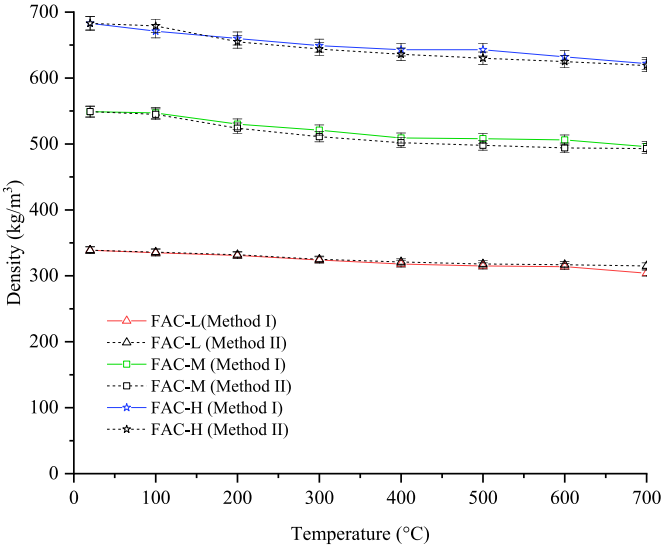

Fig. 12. Density as a function of temperature.

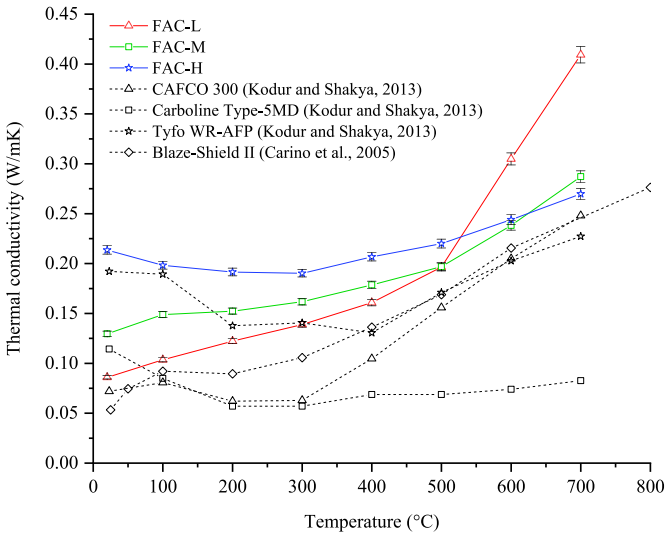

Fig. 13. Thermal conductivity as a function of temperature.

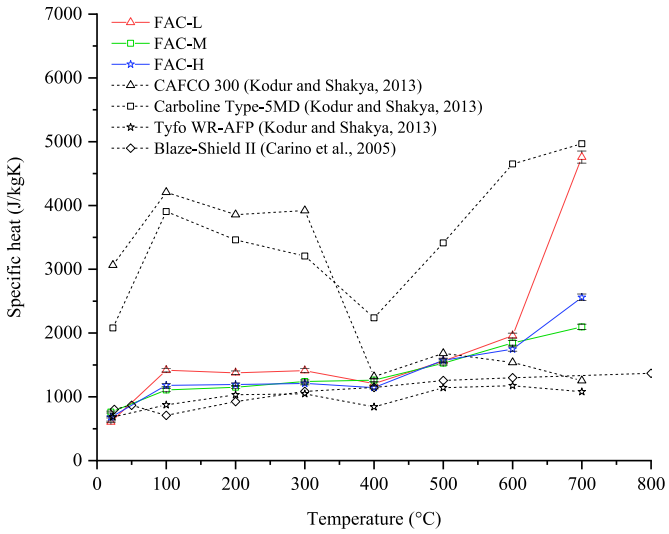

Fig. 14. Specific heat as a function of temperature.

medium-density FAC-M and low-density FAC-L developed in this study. This could be explained by the high porosity of the two SFRMs. For a porous material (such as a SFRM), its overall thermal conductivity is mainly affected by heat transfer through conduction in the solid phase and gas phase in pores and radiation across pores (Bentz et al., 2006; Wakili et al., 2015). The radiation contribution to the overall thermal conductivity is proportional to the pore size and the third power of the temperature in the pore. Therefore, the radiation contribution is very small in the beginning but increases dramatically with increasing temperature. The increase in radiation contribution could outweigh the reduction in conduction contribution (because of moisture loss), leading to the increased thermal conductivity of a SFRM. This has also been reported for Blaze-Shield II (Carino et al., 2005). It is worth noting that an opposite decreasing trend was reported by Kodur and Shakya (2013) for Carboline Type-5MD. This could be attributable to the high amount of moisture in the gypsum binder of this SFRM, making this effect dominant up to 300 °C.

In the temperature range of 300–700 °C, all SFRMs developed in this study had increased thermal conductivities with increasing temperature. This was due to the increased radiation contribution from pores. Similar observations have been reported for commercially-available SFRMs. In particular, the thermal conductivity of FAC-L increased dramatically at 600 and 700 °C. This could be explained by the thermal degradation of BST aggregates and increased pore size in FAC-L. Accordingly, the radiation contribution from pores increased significantly (Bentz et al., 2006).

Among the three developed SFRMs, the thermal conductivity of FAC-H was the least sensitive to temperature because of its relatively small pore size. Compared to the commercially available SFRMs, the SFRMs developed in this study generally had slightly higher thermal conductivities. This was because those commercial products (except Blaze-Shield II) contain a high proportion (30−35%) of vermiculite with low thermal conductivity (Kodur and Shakya, 2013).

3.3.7. *Specific heat*

The specific heat (c) of a SFRM is shown in Fig. 14 as a function of temperature. The c-value was calculated from the volumetric heat capacity (c_{vol}) divided by the density (ρ) at that temperature (Hurley et al., 2015). The high-temperature density was determined using Method I described in Section 3.3.5. At room temperature, the obtained c-values (606–760 J/kg K) of the three developed SFRMs were comparable, where the specific heat of FAC-L was slightly lower than those of FAC-M and FAC-H.

As SFRM is a compound material, its specific heat is mainly dependent on the amount of solid material and water present inside the pores. At elevated temperatures, the specific heat evolution of SFRM is significantly affected by changes in water content (moisture and bound water) and mass. It has been well documented that dehydration and moisture loss contribute to the increase of specific heat for cementitious materials (Lieff and Stumpf, 1983). In the temperature range of 100–300 °C, the c-value of a developed SFRM increased due to the evaporation of free water in the SFRM (Kodur and Shakya, 2013). At 400 °C, the c-values of FAC-L and FAC-H decreased slightly after the evaporation of free water, whereas the specific heat of FAC-M remained stable. Beyond 400 °C, the c-values of all three SFRMs increased again, which was attributed to the release of chemically bound water present in the SFRMs. It is worth noting that the c-value of FAC-L increased dramatically at 700 °C, which was due to a sudden mass loss, as a result of the thermal degradation and melting of BST aggregates.

Compared to the commercially available gypsum-based SFRMs (CAFCO 300 and Carboline Type-5MD), the SFRMs developed in this study exhibited considerably lower specific heat capacities. This is because those commercial products have a high gypsum content (70–75%), in which the water could evaporate and absorb a large amount of heat (Kodur and Shakya, 2013). Nevertheless, the specific heat versus temperature curves of the current SFRMs is similar to those of the commercially available Portland cement-based SFRM (Blaze-Shield II) and gypsum/cement-based SFRM (Tyfo WR-AFP).

4. Conclusions

This study has confirmed the feasibility of using fly ash and expanded glass to manufacture SFRMs. As the developed SFRMs exhibited excellent mechanical and thermal properties, the potential commercialisation and cleaner production of the SFRMs can have positive socio-economic and environmental impacts by providing a viable solution to effectively disposing of fly ash and waste glass in Australia. The following conclusions can be drawn from this study.

(1) The use of fly ash blended cement (FAC) could significantly reduce Portland cement usage by 81%. Fly ashes from four different power plants have been tried to make FAC binders, and the obtained 28-day compressive strengths were relatively high (33.8−46.3 MPa). Using FAC instead of Portland cement could reduce carbon emissions by 68.4% and save costs by 38.4% in the Australian context.
(2) Three SFRMs with different densities were developed utilising FAC and expanded glass. All the developed SFRMs met the

requirements for density, compressive strength, bond strength, and non-combustibility.

(3) Thermal properties (i.e., thermal conductivity and specific heat) of SFRMs are greatly affected by the type and content of binders and lightweight fillers. During heat exposure, free water and chemically bound water in the SFRMs could evaporate. Decarbonisation of dolomite and calcite in the binder was also observed. Furthermore, the thermal degradation of EPS aggregates had a significant influence on the thermal properties of the low-density SFRM. In general, the thermal properties of the developed SFRMs were comparable to those of commercially available cement-based SFRMs in the same density group.

This study has established the practicality and advantages of producing greener and more cost-effective SFRMs for protecting buildings and infrastructure against fire. Despite the extensive investigation of the material behaviour of SFRMs in this study, further research is needed to understand the performance of structural members and systems protected by the developed SFRMs under real fire conditions. Guidelines should also be developed to guide the use of the SFRMs in practice.

CRediT authorship contribution statement

Qingtao Huang: Investigation, Methodology, Writing – original draft. **Zhong Tao:** Supervision, Methodology, Resources, Conceptualization, Funding acquisition, Writing – review & editing. **Zhu Pan:** Supervision, Validation. **Laurel George:** Investigation, Validation. **Richard Wuhrer:** Validation. **Maroun Rahme:** Validation, Resources.

Declaration of competing interest

The authors declare the following financial interests/personal relationships which may be considered as potential competing interests: Zhong Tao reports financial support was provided by Australian Research Council.

Data availability

Data will be made available on request.

Acknowledgements

The authors gratefully acknowledge the financial support of the Australian Research Council (Grants No. IH150100006 and No. LP160101484). Special thanks are given to Dr Daniel Fanna from Advanced Materials Characterisation Facility (AMCF) at Western Sydney University.

References

A/D Fire Protection Systems, 2017a. Southwest Type 5GP product data sheet. http://www.adfire.com/media/83020/southwest-type-5gp-pds.pdf. (Accessed 12 June 2023).

A/D Fire Protection Systems, 2017b. Southwest Type 7GP product data sheet. http://www.adfire.com/media/83026/southwest-type-7gp-pds.pdf. (Accessed 12 June 2023).

Aegion Corporation, 2018. Tyfo WR-AFP product data sheet. https://www.carboline.com/products/product-details/SOUTHWEST-TYPE-5MD. (Accessed 12 June 2023).

Arslan, M.E., Celebi, E., 2019. An experimental study on cyclic behavior of aerated concrete block masonry walls retrofitted with different methods. Construct. Build. Mater. 200, 226–239.

Ash Development Association of Australia, 2022. Annual Production and Utilisation Survey Report: 2021. Wollongong, Australia.

Aslani, F., Ma, G., 2018. Normal and high-strength lightweight self-compacting concrete incorporating perlite, scoria, and polystyrene aggregates at elevated temperatures. J. Mater. Civ. Eng. 30 (12), 04018328.

ASTM International, 2015. E761/E761M-92(2015) Standard Test Method for Compressive Strength of Sprayed Fire-Resistive Material Applied to Structural Members. West Conshohocken, Pennsylvania, USA.

ASTM International, 2016. C109/C109M-16a Standard Test Method for Compressive Strength of Hydraulic Cement Mortars West Conshohocken. Pennsylvania, USA.

ASTM International, 2018. E2652-18 Standard Test Method for Assessing Combustibility of Materials Using a Tube Furnace with a Cone-Shaped Airflow Stabilizer at 750°C. West Conshohocken, Pennsylvania, USA.

ASTM International, 2019a. C618-19 Standard Specification for Coal Fly Ash and Raw or Calcined Natural Pozzolan for Use in Concrete. West Conshohocken, Pennsylvania, USA.

ASTM International, 2019b. E605/E605M-19 Standard Test Methods for Thickness and Density of Sprayed Fire-Resistive Material (SFRM) Applied to Structural Members. West Conshohocken, Pennsylvania, USA.

ASTM International, 2019c. E736/E736M-19 Standard Test Method for Cohesion/Adhesion of Sprayed Fire-Resistive Materials Applied to Structural Members. West Conshohocken, Pennsylvania, USA.

Bentz, D.P., 2010. Fire resistive materials: thermal barriers between fires and structures. In: Proceedings of the 30th International Thermal Conductivity Conference and the 18th International Thermal Expansion Symposium, pp. 108–119. PA, USA.

Bentz, D.P., Prasad, K., 2007. Thermal performance of fire resistive materials: I. Characterization with respect to thermal performance models. In: NISTIR 740. US Department of Commerce, Technology Administration, National Institute of Standards and Technology.

Bentz, D.P., Prasad, K.R., Yang, J.C., 2006. Towards a methodology for the characterization of fire resistive materials with respect to thermal performance models. Fire Mater. 30 (4), 311–321.

Bernardo, E., Scarinci, G., Edme, E., Michon, U., Planty, N., 2009. Fast-sintered gehlenite glass–ceramics from plasma-vitrified municipal solid waste incinerator fly ashes. J. Am. Ceram. Soc. 92 (2), 528–530.

Beyond Zero Emissions, 2017. Zero Carbon Industry Plan: Rethinking Cement. Fitzroy, Victoria, Australia.

Braxtan, N.L., Pessiki, S., 2011. Bond performance of SFRM on steel plates subjected to tensile yielding. J. Fire Protect. Eng. 21 (1), 37–55.

Bumanis, G., Bajare, D., Korjakins, A., 2013. Mechanical and thermal properties of lightweight concrete made from expanded glass. J. Sustain. Architect. Civ. Eng. 2 (3), 19–25.

Carboline, 2018. Pryrolite 15 product data sheet. https://www.mediator.com.ro/tech/en/Pyrolite_15_PDS_1_06.pdf. (Accessed 12 June 2023).

Carboline, 2021. Type 5MD product data sheet. https://www.carboline.com/products/product-details/SOUTHWEST-TYPE-5MD. (Accessed 12 June 2023).

Carino, N.J., Starnes, M.A., Gross, J.L., Yang, J.C., Kukuck, S.R., Prasad, K.R., Bukowski, R.W., 2005. Passive Fire Protection, Federal Building and Fire Safety Investigation of the World Trade Center Disaster, Report No. NIST NCSTAR 1-6A. U. S. Government Printing Office, Washington, USA.

Carvill, J., 1993. Chapter 6 - Engineering Materials, Mechanical Engineer's Data Handbook. Butterworth-Heinemann, Oxford, UK, pp. 218–266.

Doval, M., Palou, M., Mojumdar, S., 2006. Hydration behavior of C2S and C2AS nanomaterials, synthetized by sol–gel method. J. Therm. Anal. Calorim. 86 (3), 595–599.

Fořt, J., Černý, R., 2018. Carbon footprint analysis of calcined gypsum production in the Czech Republic. J. Clean. Prod. 177, 795–802.

gcp applied technologies, 2019. MONOKOTE MK-6s product data sheet https://gcpat.com/sites/gcpat.com/files/pdf/current/resource/66151_monokote_mk_6s_en.pdf. (accessed 12 June 2023).

Gewain, R.G., Iwankiw, B.R., Alfawakhiri, F., Frater, G., 2006. Facts for Steel Buildings. Canadian Institute of Steel Construction, Markham, Canada.

Gunasekara, C., Setunge, S., Law, D.W., 2017. Long-term mechanical properties of different fly ash geopolymers. ACI Struct. J. 114 (3), 743–752.

Han, X., Lou, Z., Yuan, C., Wu, X., Liu, J., Weng, F., Li, Y., 2022. Study on the effect of two-step saturated steam heat treatment process on the properties of reconstituted bamboo. J. Renew. Mater. 10 (12), 3313–3334.

Hewlett, P.C., Liska, M., 2017. Lea's Chemistry of Cement and Concrete. Butterworth-Heinemann.

Huang, Q., Tao, Z., Pan, Z., Wuhrer, R., Rahme, M., 2022. Use of sodium/potassium citrate to enhance strength development in carbonate-activated hybrid cement. Construct. Build. Mater. 350, 128913.

Hurley, M.J., Gottuk, D.T., Hall Jr., J.R., Harada, K., Kuligowski, E.D., Puchovsky, M., Watts Jr., J.M., Wieczorek, C.J., 2015. SFPE Handbook of Fire Protection Engineering. Springer.

Islam, M., Rubieyat, B.A., 2018. Fire protection of steel structure: an overall review. World Sci. News 102, 131–145.

ISOLATEK International, 2018a. CAFCO 300 technical data sheet. http://isolatek.com/productinfo/TDS/CAFCO%20300_C_TDS_07-18.pdf. (Accessed 12 June 2023).

ISOLATEK International, 2018b. CAFCO 400 technical data sheet. http://isolatek.com/productinfo/TDS/CAFCO%20400_C-TDS_07-18.pdf. (Accessed 12 June 2023).

ISOLATEK International, 2018c. CAFCO Blaze-shield II technical data sheet. http://isolatek.com/productinfo/TDS/CAFCO%20BLAZESHIELD%20II_C-TDS_07-18.pdf. (Accessed 12 June 2023).

ISOLATEK International, 2018d. CAFCO Fendolite MII technical data sheet. http://isolatek.com/productinfo/TDS/CAFCO%20FENDOLITE%20M-II%20C-TDS_07-18.pdf. (Accessed 12 June 2023).

ISOLATEK International, 2019. Physical Performance Standards for Spray-Applied Fire Resistive Materials (SFRMs). ISOLATEK International. Netcong, NJ, USA.

Jowsey, A., Scott, P., 2014. An overview of optimising passive fire protection using a limiting temperature by structural assessment. J. Struct. Fire Eng. 5 (1), 25–34.

Kodur, V., Arablouei, A., 2015. Effective properties of spray-applied fire-resistive material for resistance to cracking and delamination from steel structures. Construct. Build. Mater. 84, 367–376.

Kodur, V., Shakya, A.M., 2013. Effect of temperature on thermal properties of spray applied fire resistive materials. Fire Saf. J. 61, 314–323.

Kodur, V., Kumar, P., Rafi, M.M., 2019. Fire hazard in buildings: review, assessment and strategies for improving fire safety. PSU Res. Rev. 4 (1), 1–23.
Kotsis, I., Balogh, A., 1989. Synthesis of wollastonite. Ceram. Int. 15 (2), 79–85.
Leong, H.Y., Ong, D.E.L., Sanjayan, J.G., Nazari, A., 2016. Suitability of Sarawak and Gladstone fly ash to produce geopolymers: a physical, chemical, mechanical, mineralogical and microstructural analysis. Ceram. Int. 42 (8), 9613–9620.
Lieff, M., Stumpf, F.M., 1983. Fire Resistive Coatings: the Need for Standards: a Symposium. ASTM International.
Ma, C., Long, G., Shi, Y., Xie, Y., 2018. Preparation of cleaner one-part geopolymer by investigating different types of commercial sodium metasilicate in China. J. Clean. Prod. 201, 636–647.
Ma, L., Su, X., Xi, Y., Wei, J., Liang, X., Zhu, J., He, H., 2019. The structural change of vermiculite during dehydration processes: a real-time in-situ XRD method. Appl. Clay Sci. 183, 105332.
Maddalena, R., Roberts, J.J., Hamilton, A., 2018. Can Portland cement be replaced by low-carbon alternative materials? A study on the thermal properties and carbon emissions of innovative cements. J. Clean. Prod. 186, 933–942.
Majerová, M., Prnová, A., Plško, A., Švančárek, P., Valúchová, J., Klement, R., Galusek, D., 2020. Crystallization kinetics of gehlenite glass microspheres. J. Therm. Anal. Calorim. 142, 1003–1010.
MasterFormat, 2011. United Facilities Guide Specification, Section 07 81 00 Spray-Applied Fireproofing. Department of Defense, USA.
McDonald, L.J., Carballo-Meilan, M.A., Chacartegui, R., Afzal, W., 2022. The physicochemical properties of Portland cement blended with calcium carbonate with different morphologies as a supplementary cementitious material. J. Clean. Prod. 338, 130309.
McLellan, B.C., Williams, R.P., Lay, J., Van Riessen, A., Corder, G.D., 2011. Costs and carbon emissions for geopolymer pastes in comparison to ordinary Portland cement. J. Clean. Prod. 19 (9–10), 1080–1090.
O'Brien, K.R., Ménaché, J., O'Moore, L.M., 2009. Impact of fly ash content and fly ash transportation distance on embodied greenhouse gas emissions and water consumption in concrete. Int. J. Life Cycle Assess. 14 (7), 621–629.
Poraver, 2019. Expanded glass technical data sheet. https://poraver.com/en/poraver/. (Accessed 12 June 2023).
Ramli Sulong, N.H., Mustapa, S.A.S., Abdul Rashid, M.K., 2019. Application of expanded polystyrene (EPS) in buildings and constructions: a review. J. Appl. Polym. Sci. 136 (20), 47529.
Rodriguez, E.T., Garbev, K., Merz, D., Black, L., Richardson, I.G., 2017. Thermal stability of C-S-H phases and applicability of Richardson and Groves' and Richardson C-(A)-S-H(I) models to synthetic C-S-H. Cement Concr. Res. 93, 45–56.
Sha, W., Pereira, G., 2001. Differential scanning calorimetry study of ordinary Portland cement paste containing metakaolin and theoretical approach of metakaolin activity. Cement Concr. Compos. 23 (6), 455–461.
Shan, Y., Liu, Z., Guan, D., 2016. CO_2 emissions from China's lime industry. Appl. Energy 166, 245–252.
Standards Australia, 2010. AS 3972-2010 Portland and Blended Cements. Sydney, Australia.
Standards Australia, 2016. AS 1530.1-1994 (R2016) Methods for Fire Tests on Building Materials, Components and Structures - Combustibility Test for Materials. Sydney, Australia.
Strydom, C., Hudson-Lamb, D., Potgieter, J., Dagg, E., 1995. The thermal dehydration of synthetic gypsum. Thermochim. Acta 269, 631–638.
Sweeney, J., Htut, T., Huen, W.Y., Vimonsatit, V., Ng, T., 2017. Investigating amorphous composition mix design performance and properties of fly ash-based geopolymer. Electron. J. Struct. Eng. 17, 33–42.
Valverde, J.M., Perejon, A., Medina, S., Perez-Maqueda, L.A., 2015. Thermal decomposition of dolomite under CO_2: insights from TGA and in situ XRD analysis. Phys. Chem. Chem. Phys. 17 (44), 30162–30176.
Wakili, K.G., Hugi, E., Karvonen, L., Schnewlin, P., Winnefeld, F., 2015. Thermal behaviour of autoclaved aerated concrete exposed to fire. Cement Concr. Compos. 62, 52–58.
White, C.C., Tan, K.T., Hunston, D.L., Byrd, E.W., 2016. Elevated temperature adhesion testing of spray-applied fire-resistive materials. Fire Mater. 40 (4), 519–534.
Xie, Y.D., Lin, X.J., Ai, H.H., Ji, T., 2020. Effect of expanded perlite or expanded vermiculite on performance of magnesium potassium phosphate cement-based refractory. ACI Mater. J. 117 (3), 217–223.
Yoder Jr., H.S., 1950. Stability relations of grossularite. J. Geol. 58 (3), 221–253.
Zhang, Q., Ye, G., 2012. Dehydration kinetics of Portland cement paste at high temperature. J. Therm. Anal. Calorim. 110 (1), 153–158.